Physics – Uspekhi **62** (9) 910 – 919 (2019)

PHYSICS OF OUR DAYS

PACS numbers: **12.20. – m**, **12.60. – i**, **13.60. – r**

Equivalent photons in proton–proton and ion–ion collisions at the Large Hadron Collider

M I Vysotsky, E V Zhemchugov

DOI: https://doi.org/10.3367/UFNe.2018.07.038389

Contents

Abstract. The equivalent photon approximation is used to calculate fiducial cross sections for dimuon production in ultraperipheral proton–proton and lead–lead collisions. Analytic formulas taking experimental cuts into account are derived. The results are compared with the measurements reported by the ATLAS collaboration.

Keywords: equivalent photon approximation, Large Hadron Collider

1. Introduction

This year marks the 111th anniversary of the birth of L D Landau. We here review the modern state of the problem that Landau and Ye M Lifshitz considered for the first time in 1934 in calculating the cross section of production of e^+e^- pairs in collisions of ultrarelativistic heavy ions [1]. We show that this problem is still of interest.

Despite all efforts, the Large Hadron Collider (LHC) has so far failed to find any signatures of a New Physics. For this reason, those scenarios of the emergence of the New Physics that seemed to be less plausible when the LHC was constructed are now becoming increasingly attractive. The LHC was designed as a hadron–hadron collider, but it can also be considered a photon–photon collider in which photons are produced in ultraperipheral collisions of hadrons. This idea is far from new: it was analyzed in detail during construction and operation of the RHIC (Relativistic Heavy Ion Collider) and the LHC [2–16]. But because it was generally believed that the probability of the emergence of a New Physics signal is significantly higher in collisions of hadrons, especially regarding Higgs boson properties, hadrons were discussed much more actively and were prioritized in the LHC experimental program. Given that a two-year maintenance period began at the LHC in late 2018, it is now an appropriate time to examine photon–photon collisions at the LHC as a source of possible New Physics events: if required, it will enable making changes to the design of detectors and possibly, allocating more time in the LHC experimental program to the exploration of heavy ion collisions.

The Feynman diagram of an ultraperipheral collision in the leading approximation is shown in Fig. 1; lead nuclei can be replaced with any charged particles. A specific feature of the ultraperipheral collision is that charged particles maintain their integrity after the collision. They do not acquire a large transverse momentum, and it is therefore difficult to detect them at the main detectors, ATLAS (A Toroidal LHC ApparatuS) and CMS (Compact Muon Solenoid); however, additional detectors are available that are designed for small scattering angles for both ATLAS and CMS (the ATLAS forward proton detector [17] and the CMS–TOTEM precision proton spectrometer [18]). Nevertheless, ultraperipheral collisions can be observed without these additional detectors by detecting the particles that are produced in the collisions.

M I Vysotsky[1, 2, 3, a], **E V Zhemchugov**[3, 1, b]
[1] National Research Center Kurchatov Institute, Alikhanov Institute of Theoretical and Experimental Physics, ul. B. Cheremushkinskaya 25, 117218 Moscow, Russian Federation
[2] National Research University Higher School of Economics, ul. Myasnitskaya 20, 101000 Moscow, Russian Federation
[3] National Research Nuclear University MEPhI, Kashirskoe shosse 31, 115409 Moscow, Russian Federation
E-mail: [a] vysotsky@itep.ru, [b] zhemchugov@itep.ru

Received 9 July 2018
Uspekhi Fizicheskikh Nauk **189** (9) 975 – 984 (2019)
DOI: https://doi.org/10.3367/UFNr.2018.07.038389
Translated by M Zh Shmatikov; edited by A M Semikhatov

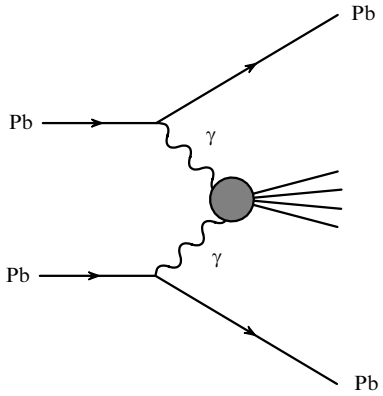

Figure 1. Feynman diagram for an ultraperipheral collision of lead nuclei.

We compare collisions of protons and collisions of lead nuclei as potential sources of New Physics events. The LHC integrated luminosity in collisions of protons that has been gathered during the second stage of LHC operation (Run 2) is now more than 150 fb^{-1} [19, 20]. The integrated LHC luminosity in collisions of lead nuclei gathered in heavy-ion runs was 0.7 nb^{-1} in 2015 [21] and 1.8 nb^{-1} in 2018 [19]. The cross section of an ultraperipheral collision is proportional to Z^4, where Z is the particle charge. The charge of lead is $Z = 82$, and therefore, if a New Physics exists that manifests itself in collisions of photons, the number of events where it will be exhibited at Run 2 is $(150\ \text{fb}^{-1})/(82^4 \times 2.5\ \text{nb}^{-1}) \approx 1.3$ times larger than in heavy ion collisions in 2015 and 2018. However, the duration of Run 2 was more than 500 days (excluding 2015, when the luminosity gathered in proton collisions was a mere 4.2 fb^{-1}), while heavy ion collisions occurred for about 45 days. Because the cross section increases as Z^4, the search for a New Physics in ultraperipheral collisions of heavy ions at the LHC is very attractive; the luminosity in ion–ion collisions can also be increased.

The cross section of particle production in ultraperipheral collisions is usually calculated using the equivalent photon approximation (EPA) [1, 22–24] (see also [25–28]). To make a comparison with experimental data, the phase volume of produced particles should be constrained with experimental cutoffs that are introduced to reduce the background and take blind spots of detectors into account. The cross section with the cutoffs taken into account (the fiducial cross section) is usually computed on the basis of the total cross section using the Monte Carlo method (see, e.g., the SuperCHIC Monte Carlo event generator [29]). The EPA enables application of the experimental cutoffs in an analytic way, and hence the use of the Monte Carlo method is often not needed.

We here use the EPA to calculate the cross section of the $\text{pp}(\gamma\gamma) \to \text{pp}\mu^+\mu^-$ reaction. Experimental constraints of three kinds are then applied to the phase space of this reaction:

1) on the invariant mass of the muon pair $\sqrt{s}$: $\hat{s}_{\min} < s < \hat{s}_{\max}$;

2) on the transverse momentum of a muon p_{T}: $p_{\text{T}} > \hat{p}_{\text{T}}$;

3) on muon pseudorapidity η: $|\eta| < \hat{\eta}$.

Numerical values of these constraints vary depending on the specific experiment and measurement setup. The analytic formulas derived here are used to describe the experimental data obtained by the ATLAS collaboration [30]. In that measurement, the bound $\hat{s}_{\min}$ was set equal to 12 GeV to exclude the contribution from decays of vector mesons to $\mu^+\mu^-$ (the heaviest vector mesons belong to the family of Υ mesons); $\hat{s}_{\max} = 70$ GeV, $\hat{p}_{\text{T}} = 6$ or 10 GeV depending on the invariant mass; and the bound $\hat{\eta} = 2.4$ ensures that the muon hits the muon spectrometer.

The same formulas are used to calculate the cross section of the $\text{PbPb}(\gamma\gamma) \to \text{PbPb}\mu^+\mu^-$ reaction with the experimental cutoffs used in [31].

2. Cross section of $\mu^+\mu^-$ production without experimental cutoffs

The distribution of equivalent photons produced by a moving ultrarelativistic particle with the charge Ze has the form

$$n(\mathbf{q})\,\mathrm{d}^3q = \frac{Z^2\alpha}{\pi^2}\,\frac{\mathbf{q}_\perp^2}{\omega q^4}\,\mathrm{d}^3q = \frac{Z^2\alpha}{\pi^2\omega}\,\frac{\mathbf{q}_\perp^2}{(\mathbf{q}_\perp^2 + (\omega/\gamma)^2)^2}\,\mathrm{d}^3q\,, \quad (1)$$

where q is the photon 4-momentum, $\mathbf{q}_\perp$ is its transverse component, ω is the photon energy, and γ is the Lorentz factor of the particle. For a proton with the energy $E = 6.5$ TeV, $\gamma = E/m_{\text{p}} \approx 6.93 \times 10^3$. To derive the equivalent-photon spectrum, Eqn (1) must be integrated over the transverse momentum up to a certain value of $\hat{q}$. The value of $\hat{q}$ should be chosen such that the initial particle does not disintegrate as a result of emitting a photon with this momentum. For a proton, $\hat{q} = 0.20$ GeV (see Appendix A). In the limit $\omega \ll \hat{q}\gamma$, the equivalent-photon spectrum acquires the form

$$n(\omega)\,\mathrm{d}\omega = \frac{2Z^2\alpha}{\pi}\ln\left(\frac{\hat{q}\gamma}{\omega}\right)\frac{\mathrm{d}\omega}{\omega}\,. \quad (2)$$

This simple expression allows deriving analytic formulas for the cross section of muon pair production taking experimental cutoffs into consideration.

The muon pair production in an ultraperipheral collision of protons is described in the leading approximation by the Feynman diagrams in Fig. 2. The corresponding cross section is

$$\sigma(\text{pp}(\gamma\gamma) \to \text{pp}\mu^+\mu^-) = \int_{m_\mu^2/\hat{q}\gamma}^{\hat{q}\gamma} \mathrm{d}\omega_1 \int_{m_\mu^2/\omega_1}^{\hat{q}\gamma} \mathrm{d}\omega_2\, \sigma(\gamma\gamma \to \mu^+\mu^-)\, n(\omega_1)\, n(\omega_2)\,, \quad (3)$$

where ω_1 and ω_2 are the energies of the photons,

$$\sigma(\gamma\gamma \to \mu^+\mu^-) = \frac{4\pi\alpha^2}{s}\left[\left(1 + \frac{4m_\mu^2}{s} - \frac{8m_\mu^4}{s^2}\right)\ln\frac{1+\sqrt{1-4m_\mu^2/s}}{1-\sqrt{1-4m_\mu^2/s}} - \left(1+\frac{4m_\mu^2}{s}\right)\sqrt{1-\frac{4m_\mu^2}{s}}\right] \quad (4)$$

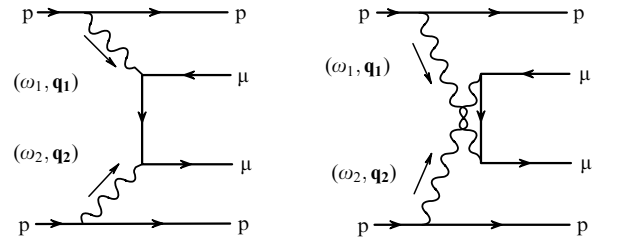

Figure 2. Leading Feynman diagrams for the $\text{pp}(\gamma\gamma) \to \text{pp}\mu^+\mu^-$ reaction.

is the Breit–Wheeler cross section [32], and $\sqrt{s}=\sqrt{4\omega_1\omega_2}$ is the invariant mass of the muons. The integration domain in Eqn (3) is shown in Fig. 3. It is helpful to change the integration variables as $\omega_1,\ \omega_2\to s,x$, where $x=\omega_1/\omega_2$. The integrals in Eqn (3) can then be represented in the form

$$\begin{aligned}&\sigma(\mathrm{pp}(\gamma\gamma)\to\mathrm{pp}\mu^+\mu^-)\\&=\int_{(2m_\mu)^2}^{(2\hat{q}\gamma)^2}\mathrm{d}s\,\sigma(\gamma\gamma\to\mu^+\mu^-)\int_{s/(2\hat{q}\gamma)^2}^{(2\hat{q}\gamma)^2/s}\frac{\mathrm{d}x}{8x}\,n\left(\sqrt{\frac{sx}{4}}\right)n\left(\sqrt{\frac{s}{4x}}\right)\\&=\frac{\alpha^2}{2\pi^2}\int_{(2m_\mu)^2}^{(2\hat{q}\gamma)^2}\frac{\mathrm{d}s}{s}\,\sigma(\gamma\gamma\to\mu^+\mu^-)\int_{s/(2\hat{q}\gamma)^2}^{(2\hat{q}\gamma)^2/s}\frac{\mathrm{d}x}{x}\\&\times\ln\frac{(2\hat{q}\gamma)^2}{sx}\ln\left[\frac{(2\hat{q}\gamma)^2}{s}x\right]\end{aligned}\tag{5}$$

(the integral over x is invariant under the substitution $x\to 1/x$). As a result, we obtain

$$\begin{aligned}&\sigma(\mathrm{pp}(\gamma\gamma)\to\mathrm{pp}\mu^+\mu^-)\\&=\frac{16\alpha^2}{3\pi^2}\int_{(2m_\mu)^2}^{(2\hat{q}\gamma)^2}\frac{\mathrm{d}s}{s}\,\sigma(\gamma\gamma\to\mu^+\mu^-)\ln^3\frac{2\hat{q}\gamma}{\sqrt{s}}\,.\end{aligned}\tag{6}$$

Because $\sigma(\gamma\gamma\to\mu^+\mu^-)$ decreases as $1/s$ if $s\gg 4m_\mu^2$, in the leading logarithmic approximation the logarithm in Eqn (6) should be taken at $s=4m_\mu^2$. We then obtain [1]

$$\sigma(\mathrm{pp}(\gamma\gamma)\to\mathrm{pp}\mu^+\mu^-)=8\times\frac{28}{27}\,\frac{\alpha^4}{\pi m_\mu^2}\ln^3\frac{\hat{q}\gamma}{m_\mu}\,.\tag{7}$$

If the mass of produced particles is significantly less than $\hat{q}$, the latter must be replaced with m in Eqn (7). [2] This is just the case of $\mathrm{e}^+\mathrm{e}^-$-pair production considered in [1]. Another difference from Eqn (37) in [1] is that the collision is considered in [1] in the laboratory frame where the nucleus is at rest and $\gamma\equiv\gamma_{\mathrm{CM}}=(\gamma_{\mathrm{lab}}/2)^{1/2}$.

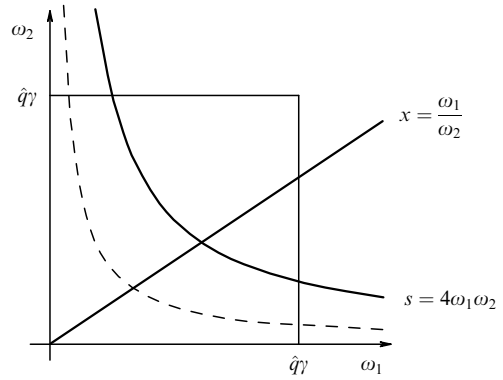

Figure 3. The integration domain in (3). The dashed line corresponds to $s=4m_\mu^2$. The integration domain is contained within the square above the dashed line.

[1] An incorrect spectrum of equivalent photons was used in Eqn (1.4) in [33] (the term $\ln^2(E/m_\mathrm{e})$ in the integrand should be replaced with the product $\ln(E/\omega_1)\ln(E/\omega_2)$), which resulted in a wrong factor 3/2 in Eqn (5.4) and reference [23] in that paper. This error was reproduced later in Eqn (5.4) in [26]. A discussion of such errors, which frequently occur in applying the EPA, can be found in the second footnote on page 256 in [28].

[2] If τ-leptons are produced, the $\hat{q}/m_\tau$ factor persists and suppresses the cross section.

For collisions of protons with an energy of 13 TeV at the LHC,

$$\sigma(\mathrm{pp}(\gamma\gamma)\to\mathrm{pp}\mu^+\mu^-)\approx 0.22\,\mu\mathrm{b}.\tag{8}$$

3. Cross section of $\mu^+\mu^-$ production with experimental cutoffs taken into account

3.1 Constraints on the invariant mass of a $\mu^+\mu^-$ pair

The invariant mass can be constrained in a trivial way: it is sufficient to change the limits of integration over s in Eqn (5). For $(2m_\mu)^2\leqslant\hat{s}_{\min}<s<\hat{s}_{\max}\leqslant(2\hat{q}\gamma)^2$,

$$\begin{aligned}&\sigma^{(\hat{s})}_{\mathrm{fid}}(\mathrm{pp}(\gamma\gamma)\to\mathrm{pp}\mu^+\mu^-)\\&=\int_{\hat{s}_{\min}}^{\hat{s}_{\max}}\mathrm{d}s\,\sigma(\gamma\gamma\to\mu^+\mu^-)\int_{s/(2\hat{q}\gamma)^2}^{(2\hat{q}\gamma)^2/s}\frac{\mathrm{d}x}{8x}\,n\left(\sqrt{\frac{sx}{4}}\right)n\left(\sqrt{\frac{s}{4x}}\right).\end{aligned}\tag{9}$$

If $\hat{s}_{\min}\gg 4m_\mu^2$, an inequality that holds for the experiments considered in Section 4, a simplified formula can be used for the Breit–Wheeler cross section:

$$\sigma(\gamma\gamma\to\mu^+\mu^-)\approx\frac{4\pi\alpha^2}{s}\left(\ln\frac{s}{m_\mu^2}-1\right)\ \text{for}\ \ s\gg 4m_\mu^2\,.\tag{10}$$

In this case,

$$\begin{aligned}&\sigma^{(\hat{s})}_{\mathrm{fid}}(\mathrm{pp}(\gamma\gamma)\to\mathrm{pp}\mu^+\mu^-)\\&=\frac{64\alpha^4}{3\pi}\int_{\hat{s}_{\min}}^{\hat{s}_{\max}}\frac{\mathrm{d}s}{s^2}\left(\ln\frac{s}{m_\mu^2}-1\right)\ln^3\frac{2\hat{q}\gamma}{\sqrt{s}}\,.\end{aligned}\tag{11}$$

According to Eqn (6.27b) in [28], the inaccuracy of Eqn (11) related to the virtuality of photons is

$$\eta\sim\left(\frac{\hat{q}^2}{\sqrt{s}_{\min}m_\mu}\right)^2\left(\ln\frac{4E^2}{s_{\min}}\right)^{-1},\tag{12}$$

where E is the energy of the colliding particles. The accuracy is very high for the production of muon–antimuon pairs, but it significantly deteriorates for the production of electron–positron pairs.

3.2 Constraints on the transverse momentum of a muon

To impose a constraint on the transverse momentum of a muon $p_\mathrm{T}>\hat{p}_\mathrm{T}$, the formula for the cross section of the $\gamma\gamma\to\mu^+\mu^-$ reaction differential in p_T [34, (88.4)] must be substituted in Eqn (9):

$$\begin{aligned}\mathrm{d}\sigma(\gamma\gamma\to\mu^+\mu^-)&=\frac{2\pi\alpha^2}{s^2}\left(\frac{s+t}{t}+\frac{t}{s+t}\right)\mathrm{d}t\\&=\frac{8\pi\alpha^2}{sp_\mathrm{T}}\,\frac{1-2p_\mathrm{T}^2/s}{\sqrt{1-4p_\mathrm{T}^2/s}}\,\mathrm{d}p_\mathrm{T}\,,\end{aligned}\tag{13}$$

where t is the Mandelstam variable, $t=-s/2\pm s/2\times(1-4p_\mathrm{T}^2/s)^{1/2}$, and muons are regarded as ultrarelativistic particles. We then arrive at the formula

$$\begin{aligned}&\sigma^{(\hat{s},\hat{p}_\mathrm{T})}_{\mathrm{fid}}(\mathrm{pp}(\gamma\gamma)\to\mathrm{pp}\mu^+\mu^-)\\&=\int_{\hat{s}_{\min}}^{\hat{s}_{\max}}\mathrm{d}s\int_{\hat{p}_\mathrm{T}}^{\sqrt{s}/2}\mathrm{d}p_\mathrm{T}\,\frac{\mathrm{d}\sigma(\gamma\gamma\to\mu^+\mu^-)}{\mathrm{d}p_\mathrm{T}}\int_{s/(2\hat{q}\gamma)^2}^{(2\hat{q}\gamma)^2/s}\frac{\mathrm{d}x}{8x}\end{aligned}\tag{14}$$

$$\begin{aligned}&\times n\left(\sqrt{\frac{sx}{4}}\right)n\left(\sqrt{\frac{s}{4x}}\right)=\frac{64\alpha^4}{3\pi}\int_{\hat{s}_{\min}}^{\hat{s}_{\max}}\frac{\mathrm{d}s}{s^2}\ln^3\frac{2\hat{q}\gamma}{\sqrt{s}}\\&\times\left(\ln\frac{1+\sqrt{1-4\hat{p}_\mathrm{T}^2/s}}{1-\sqrt{1-4\hat{p}_\mathrm{T}^2/s}}-\sqrt{1-\frac{4\hat{p}_\mathrm{T}^2}{s}}\right).\end{aligned}\tag{15}$$

3.3 Constraints on the muon pseudorapidity

The pseudorapidity is defined as $\eta = -\ln\tan(\theta/2)$, where θ is the angle between the muon momentum and the beam. Experimental pseudorapidity constraints are related to specific features of detector geometry. The ATLAS muon spectrometer is not able to detect muons with $\theta \lesssim 10^\circ$ or $\theta \gtrsim 170^\circ$, the angles that correspond to the pseudorapidity cutoff $|\eta| < 2.4$

If the invariant mass s of a muon pair is fixed, muon pseudorapidity values are determined by the ratio of photon energies x. If $x = 1$, then in the phase space region bounded by the p_T and s cutoffs used in [30] (Table 1) $\sin\theta = 2p_T/\sqrt{s}$ is always larger than 2/7. This value corresponds to the interval $17^\circ \lesssim \theta \lesssim 163^\circ$. Thus, the η cutoff does not result in a reduction in the number of detected events of muon pair production. But if $x \ll 1$ or $x \gg 1$, muons move parallel to the proton beam and escape from the detector undetected. Consequentially, the pseudorapidity cutoff can be converted in a natural way into an x constraint:

$$|\eta| < \hat{\eta} \Rightarrow \frac{1}{\hat{x}} < x < \hat{x}\,, \tag{16}$$

where

$$\hat{x} = \exp(2\hat{\eta})\frac{1-\sqrt{1-4p_T^2/s}}{1+\sqrt{1-4p_T^2/s}} \tag{17}$$

(see Appendix B). From this equation, we obtain a formula for the fiducial cross section with all the experimental constraints taken into account:

$$\sigma_{\rm fid}^{(\hat{s},\hat{p}_T,\hat{\eta})}(pp(\gamma\gamma)\to pp\mu^+\mu^-) = \int_{\hat{s}_{\min}}^{\hat{s}_{\max}} ds \int_{\hat{p}_T}^{\sqrt{s}/2} dp_T \frac{d\sigma(\gamma\gamma\to\mu^+\mu^-)}{dp_T}\int_{1/\hat{x}}^{\hat{x}}\frac{dx}{8x} \tag{18}$$

$$\times\, n\left(\sqrt{\frac{sx}{4}}\right) n\left(\sqrt{\frac{s}{4x}}\right) = \frac{4\alpha^4}{\pi}\int_{\hat{s}_{\min}}^{\hat{s}_{\max}}\frac{ds}{s^2}\int_{\hat{p}_T}^{\sqrt{s}/2}\frac{dp_T}{p_T}$$

$$\times\frac{1-2p_T^2/s}{\sqrt{1-4p_T^2/s}}\int_{1/\hat{x}}^{\hat{x}}\frac{dx}{x}\ln\frac{(2\hat{q}\gamma)^2}{sx}\ln\left(\frac{(2\hat{q}\gamma)^2}{s}x\right). \tag{19}$$

4. Comparison with experimental data

4.1 Production of a muon pair in proton collisions

The ATLAS collaboration has measured the fiducial cross section of the $pp \to pp\mu^+\mu^-$ reaction at a proton collision energy of 13 TeV ($\gamma = 6.93\times10^3$) with the integrated luminosity 3.2 fb^{-1} [30]. The experimental constraints are displayed in Table 1. The result of measurements is

$$\sigma_{\rm fid}^{\rm exper}(pp\to pp\mu^+\mu^-) = 3.12 \pm 0.07\,({\rm stat.}) \pm 0.10\,({\rm syst.})\ {\rm pb}\,. \tag{20}$$

Table 1. Phase-space constraints of the $pp(\gamma\gamma) \to pp\mu^+\mu^-$ reaction used in [30].

Range of invariant masses of muons	Transverse momentum of muon	Muon pseudorapidity
$12 < \sqrt{s} < 30$ GeV $30 < \sqrt{s} < 70$ GeV	$p_T > 6$ GeV $p_T > 10$ GeV	$\|\eta\| < 2.4$

Table 2. Cross section of the $pp(\gamma\gamma) \to pp\mu^+\mu^-$ reaction with the experimental constraints, calculated using the equivalent-photon spectrum in Eqn (2) and Eqns (6), (11), (15), and (19).

Constraints	Cross section, pb	
Without constraints	1.7×10^5	
$12 < \sqrt{s} < 30$ GeV $30 < \sqrt{s} < 70$ GeV	54.1 5.66	59.7
$12 < \sqrt{s} < 30$ GeV, $p_T > 6$ GeV $30 < \sqrt{s} < 70$ GeV, $p_T > 10$ GeV	5.38 0.91	6.29
$12 < \sqrt{s} < 30$ GeV, $p_T > 6$ GeV, $\|\eta\| < 2.4$ $30 < \sqrt{s} < 70$ GeV, $p_T > 10$ GeV, $\|\eta\| < 2.4$	2.85 0.50	3.35

The results obtained if the experimental constraints are applied one by one to the cross section of this reaction are shown in Table 2. The fiducial cross section is

$$\sigma_{\rm fid}^{(\hat{s},\hat{p}_T,\hat{\eta})}\left(pp(\gamma\gamma)\to pp\mu^+\mu^-\right) = 3.35\ {\rm pb}\,, \tag{21}$$

which agrees with Eqn (20). Figure 4 displays a comparison of the cross section for several invariant mass ranges with the experimental data contained in Table 3 in [30]. [3]

Experimental results are compared in [30] with the theoretical predictions obtained using the Monte Carlo method: the SuperCHIC program [29] yields

$$\sigma_{\rm fid} = 3.45 \pm 0.05\,{\rm pb}\ [29, 30]\,, \tag{22}$$

while the EPA taking corrections due to absorption effects [35] (see Appendix C) into consideration yields

$$\sigma_{\rm fid} = 3.06 \pm 0.05\,{\rm pb}\ [30, 35]\,. \tag{23}$$

4.2 Production of a muon pair in collisions of lead nuclei

The ATLAS collaboration has measured the fiducial cross section of the $PbPb \to PbPb\,\mu^+\mu^-$ reaction at a collision energy of 5.02 TeV per nucleon pair ($\gamma = 2.69\times10^3$) with the integrated luminosity 515 μb^{-1} [31]. The following experimental constraints were used:

- on the invariant mass of a muon pair: $10 < \sqrt{s} < 100$ GeV;
- on the transverse momentum of a muon: $p_T > 4$ GeV;
- on the muon pseudorapidity: $|\eta| < 2.4$.

The result of the measurement is

$$\sigma_{\rm fid}^{\rm exper}(PbPb\to PbPb\,\mu^+\mu^-) = 32.2 \pm 0.3\,({\rm stat.})^{+4.0}_{-3.4}\,({\rm syst.})\ \mu{\rm b}\,. \tag{24}$$

A heavy nucleus can be disintegrated more easily than the proton. The maximum momentum that a proton can transfer without disintegration is $\hat{q} \approx 0.20$ GeV [see (A.8)]. The corresponding value for ^{208}Pb strongly depends on the nucleus form factor but in any case is about an order of magnitude smaller. The maximum photon energy in the leading logarithmic approximation is $2\hat{q}\gamma$. This quantity for protons colliding with an energy of 13 TeV is 2.8 TeV, while for collisions of lead nuclei that are considered in this section, it is about 100 GeV. The collisions of lead nuclei are therefore

[3] In calculating the cross section displayed in Fig. 4, equivalent-photon spectrum (2) is used. If the dipole form factor is taken into account (see Eqn (A.6) in Appendix A), the cross section increases by less than 0.5% in the energy range under consideration. The magnetic form factor [see (A.3)] increases the cross section by $\approx 6\%$.

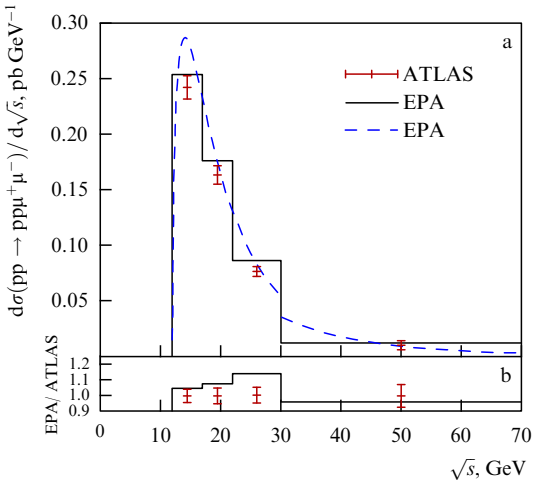

Figure 4. (a) Fiducial cross section of the $pp(\gamma\gamma) \to pp\mu^+\mu^-$ reaction for a proton collision energy of 13 TeV with the experimental constraints presented in Table 1. EPA means the equivalent photon approximation. Dots with error bars represent the experimental data displayed in Table 3 in [30]. The dashed line corresponds to the differential cross section calculated using Eqn (19). The histogram shows the differential cross section averaged over the intervals that are also displayed in Table 3 in [30]. (b) Ratio of the calculated cross section to experimental values.

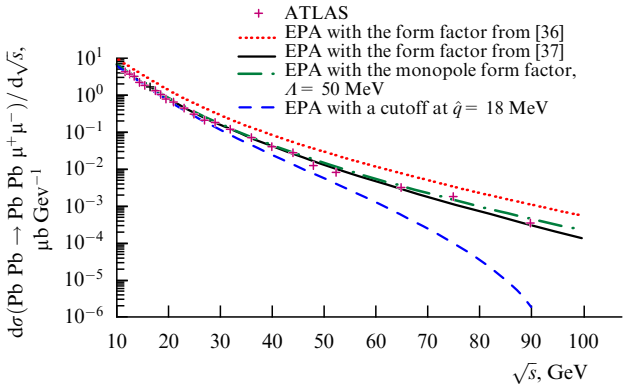

Figure 5. (Color online.) Differential fiducial cross section of the $Pb\,Pb\,(\gamma\gamma) \to Pb\,Pb\,\mu^+\mu^-$ reaction at a collision energy of 5.02 TeV per nucleon pair with the experimental constraints from [31]. Crosses show the experimental data from the left-hand plot in [31] (upper curve). The curves were plotted using Eqn (18). The red dotted line and black solid line are plotted using the equivalent-photon spectrum with form factors taken from [36, 37]. The green dashed-dotted line corresponds to the spectrum with the monopole form factor with the parameter $\Lambda = 50$ MeV. The dashed blue line is plotted using the spectrum in Eqn (2) with $\hat{q} = 18$ MeV.

much more sensitive to the momentum dependence of the form factor of colliding particles.

To calculate the fiducial cross section, Eqn (18) was used with several equivalent-photon spectra $n(\omega)$ that correspond to various form factors [36, 37]. Figure 5 displays a comparison of calculated results with the experimental data shown in the left-hand plot in Fig. 3 of [31].[4] The spectrum with the form factor determined by the Fourier–Bessel parameters from [37] (see Table 4 in Appendix A) and the spectrum with the monopole form factor with the parameter $\Lambda = 50$ MeV compare well with the experimental data. The leading logarithmic approximation with $\hat{q} = 18$ MeV [see (A.14)] exhibits good accuracy in the region of small invariant masses, while in the region of large invariant masses, it underestimates the number of equivalent photons. The reason is that the assumption $\omega \ll \hat{q}\gamma \approx 50$ GeV used in deriving Eqn (2) fails in this region. The form factor described by the Fourier–Bessel parameters from a previous study [36] (see Table 4 in Appendix A) and its approximation with the monopole form factor with the parameter $\Lambda = 80$ MeV, which is used frequently [38–40], yield a fiducial cross section that is 1.5 times larger than the measured one.

Table 3. Fiducial cross section of the $Pb\,Pb\,(\gamma\gamma) \to Pb\,Pb\,\mu^+\mu^-$ reaction with the nuclear form factor approximated using the monopole formula with $\Lambda = 50$ MeV.

Constraints	Cross section, μb
Without constraints	1.92×10^6
$10 < \sqrt{s} < 100$ GeV also $p_T > 4$ GeV also $\lvert\eta\rvert < 2.4$	264 42.5 34.6

[4] The left-hand plot in Fig. 3 in [31] contains two sets of data that correspond to two constraints on the muon-pair rapidity $Y_{\mu\mu}$. The muon pair rapidity constraint is not considered in this review. The constraint $|Y_{\mu\mu}| < 2.4$ used for the upper set of points corresponds to the constraint $|\eta| < 2.4$.

The fiducial cross section calculated using the equivalent-photon spectrum with the form factor determined by the Fourier–Bessel parameters from [37],

$$\sigma_{\rm fid}^{(\hat{s},\hat{p}_T,\hat{\eta})}(Pb\,Pb\,(\gamma\gamma) \to Pb\,Pb\,\mu^+\mu^-) = 34.4\ \mu b\,, \qquad (25)$$

compares well with experimental result (24). Results of a successive application of the constraints are presented in Table 3.

Results of the measurements are compared in [31] with the results computed using the STARLIGHT package [41]:

$$\sigma_{\rm fid}\,(Pb\,Pb\,(\gamma\gamma) \to Pb\,Pb\,\mu^+\mu^-) = 31.64 \pm 0.04\ \mu b\,[31, 41]\,. \qquad (26)$$

5. Conclusion

The LHC can be used to search for a New Physics in photon–photon collisions. The invariant mass of photons can be as large as $2\hat{q}\gamma \approx 2.8$ TeV in collisions of protons with an energy of 13 TeV and ≈ 100 GeV in collisions of lead nuclei with an energy of 5.02 TeV per nucleon pair.

The equivalent-photon approximation enables analytic calculation of the cross section taking experimental constraints into consideration. The leading logarithmic approximation [see Eqn (2)] yields accurate results and relatively simple formulas for the invariant masses that are much smaller than $\hat{q}\gamma$. If invariant masses are larger, form factors of colliding particles should be taken into account.

Although the constraints significantly decrease the number of detected events, the high luminosity of the LHC enables observation of $\mu^+\mu^-$ pair production in ultraperipheral collisions.

We are grateful to A N Rozanov for the discussion that attracted our interest to LHC results in photon collision reactions, I I Tsukerman for the helpful comments, H Terazawa for providing a reference to studies [26, 33], I F Ginzburg for a very fruitful discussion, S I Godunov for

his help in checking numerical calculations, and V A Novikov for the discussions that led to writing Appendix C. The study was supported by grant no. 16-02-00342 from the Russian Foundation for Basic Research. Sections 3 and 4 and Appendix C were created with support from grant no. 19-12-00123 from the Russian Science Foundation.

Appendix A. Constraints on equivalent-photon virtuality

We consider a charged particle at rest. Its electromagnetic field can be represented as a multitude of virtual zero-energy photons. Let $q = (0, q_x, q_y, q_z)$ be the momentum of such a virtual photon. Let then the particle move along the z-direction with a Lorentz factor $\gamma \gg 1$. The photon then acquires the energy $\omega = (\gamma^2 - 1)^{1/2} q_z$, which is approximately equal to the photon momentum in the z-direction, γq_z. The virtuality of such a photon is $-q^2 = q_x^2 + q_y^2 + q_z^2 \ll \omega^2$, owing to which it can be treated as real. This is the essence of the equivalent photon approximation.

To obtain the virtual-photon spectrum $n(\omega)$ of a particle in motion, Eqn (2), the virtual photon distribution $n(\mathbf{q})\,\mathrm{d}^3q$ in (1) should be integrated with respect to the transverse momentum $q_\perp = (q_x^2 + q_y^2)^{1/2}$. Because this integral logarithmically diverges at large $q_\perp$, it should be cut off at some value $\hat{q}$. If a proton (or nucleus) emits a virtual photon with a rather large momentum in the collision, the proton (nucleus) disintegrates. A natural estimate for the proton $\hat{q}$ is therefore the inverse radius of the proton or the quantum chromodynamics scale Λ_{QCD}, which is in the range 200–300 MeV [42, Section 9]. If an $\mathrm{e}^+\mathrm{e}^-$ pair is produced, $\hat{q} = m_\mathrm{e}$, because the contribution from the $q_\perp > m_\mathrm{e}$ region is suppressed by a power-law function.

A more rigorous derivation of the $\hat{q}$ value involves proton form factors. The Dirac form factor of a proton is [43]

$$F_1(q^2) = \frac{G_\mathrm{E}(q^2) + \tau G_\mathrm{M}(q^2)}{1+\tau}\,, \tag{A.1}$$

where $\tau = -q^2/4m_\mathrm{p}^2$, G_E is the electric form factor, G_M is the magnetic form factor,

$$G_\mathrm{E}(q^2) = \frac{1}{(1 - q^2/\Lambda^2)^2}\,, \tag{A.2}$$

$$G_\mathrm{M}(q^2) = \frac{\mu_\mathrm{p}}{(1 - q^2/\Lambda^2)^2}\,, \tag{A.3}$$

$\mu_\mathrm{p} = 2.79$ is the magnetic moment of the proton, and $\Lambda^2 = 0.71\ \mathrm{GeV}^2$. Equation (A.1) can be represented as

$$F_1(q^2) = G_\mathrm{D}(q^2)\left[1 + \frac{(\mu_\mathrm{p} - 1)\,\tau}{1+\tau}\right], \tag{A.4}$$

where $G_\mathrm{D}(q^2) \equiv G_\mathrm{E}(q^2)$ is the dipole form factor. Because $-q^2 \approx q_\perp^2$ cannot be significantly larger than Λ_{QCD}^2, $\tau \ll 1$, and the contribution of the magnetic form factor can be neglected. The derivation of Eqn (1) for the momentum distribution of equivalent photons in accordance with [34, § 99] taking the form factor into consideration yields

$$\begin{aligned} n_\mathrm{dipole}(\mathbf{q})\,\mathrm{d}^3q &= \frac{\alpha}{\pi^2}\,\frac{\mathbf{q}_\perp^2}{\omega q^4}\left(1 - \frac{q^2}{\Lambda^2}\right)^{-4}\mathrm{d}^3q \\ &= \frac{\alpha}{\pi^2\omega}\,\frac{\mathbf{q}_\perp^2}{(\omega^2/\gamma^2 + q_\perp^2)^2}\left(1 + \frac{1}{\Lambda^2}\left(\frac{\omega^2}{\gamma^2} + q_\perp^2\right)\right)^{-4}\mathrm{d}^3q. \end{aligned} \tag{A.5}$$

The equivalent-photon spectrum is

$$\begin{aligned} n_\mathrm{dipole}(\omega)\,\mathrm{d}\omega &= 2\pi\int_0^\infty n_\mathrm{dipole}(\mathbf{q}) q_\perp \mathrm{d}q_\perp \mathrm{d}\omega \\ &= \frac{\alpha}{\pi}\left[(4a+1)\ln\left(1 + \frac{1}{a}\right) - \frac{24a^2 + 42a + 17}{6(a+1)^2}\right]\frac{\mathrm{d}\omega}{\omega}, \end{aligned} \tag{A.6}$$

where $a = (\omega/\Lambda\gamma)^2$. This function monotonically decreases as ω increases. In the low-energy region $\omega \ll \Lambda\gamma$ that contains most of the photons,

$$n_\mathrm{dipole}(\omega)\,\mathrm{d}\omega \underset{a\to 0}{\longrightarrow} \frac{\alpha}{\pi}\left[2\ln\frac{\Lambda\gamma}{\omega} - \frac{17}{6}\right]\frac{\mathrm{d}\omega}{\omega}\,. \tag{A.7}$$

A comparison of this formula with Eqn (2) for $Z = 1$ yields

$$\hat{q} = \Lambda \exp\left(-\frac{17}{12}\right) \approx 200\ \mathrm{MeV}\,, \tag{A.8}$$

a value that agrees well with the assumption made that $\hat{q} \approx \Lambda_{\mathrm{QCD}}$.

The structure of a heavy nucleus form factors is more involved. The most accurate description of the ^{208}Pb form factor seems to be provided by the Fourier-transformed Bessel-function expansion of the charge density in the nucleus as a function of distance from the center [44]:

$$\rho(r) = \begin{cases} \sum_{n=1}^N a_n j_0\left(\dfrac{n\pi r}{R}\right), & r \leqslant R\,, \\ 0\,, & r \geqslant R\,, \end{cases} \tag{A.9}$$

where $j_0(x) = \sin x/x$ is the spherical Bessel function of the zeroth order, and the values of the parameters a_n and R are displayed in Table 4. The corresponding form factor has the form

$$\begin{aligned} F_\mathrm{Fourier\text{–}Bessel}(q^2) &= \frac{\int \rho(r)\exp(\mathrm{i}\,\mathbf{qr})\,\mathrm{d}^3r}{\int \rho(r)\,\mathrm{d}^3r} \\ &= \frac{\sin qR}{qR}\sum_{n=1}^N \frac{(-1)^n a_n}{n^2\pi^2 - q^2R^2}\left(\sum_{n=1}^N \frac{(-1)^n a_n}{n^2\pi^2}\right)^{-1}. \end{aligned} \tag{A.10}$$

The form factor of a heavy nucleus is often approximated with the monopole formula

$$F_\mathrm{monopole}(q^2) \approx \frac{1}{1 - q^2/\Lambda^2}\,. \tag{A.11}$$

The corresponding spectrum of equivalent photons is

$$\begin{aligned} &n_\mathrm{monopole}(\omega)\,\mathrm{d}\omega \\ &\quad= \frac{Z^2\alpha}{\pi}\left[(2a+1)\ln\left(1 + \frac{1}{a}\right) - 2\right]\frac{\mathrm{d}\omega}{\omega}\,. \end{aligned} \tag{A.12}$$

In the low-energy region,

$$n_\mathrm{monopole}(\omega)\,\mathrm{d}\omega \underset{a\to 0}{\longrightarrow} \frac{Z^2\alpha}{\pi}\left[2\ln\frac{\Lambda\gamma}{\omega} - 2\right]\frac{\mathrm{d}\omega}{\omega}\,, \tag{A.13}$$

yielding

$$\hat{q} = \Lambda\exp(-1)\,. \tag{A.14}$$

For $\Lambda = 80$ MeV used in [38–40], we obtain $\hat{q} \approx 30$ MeV. This value of Λ seems to describe outdated data, however. Figure 6 shows a comparison of the monopole form factor with

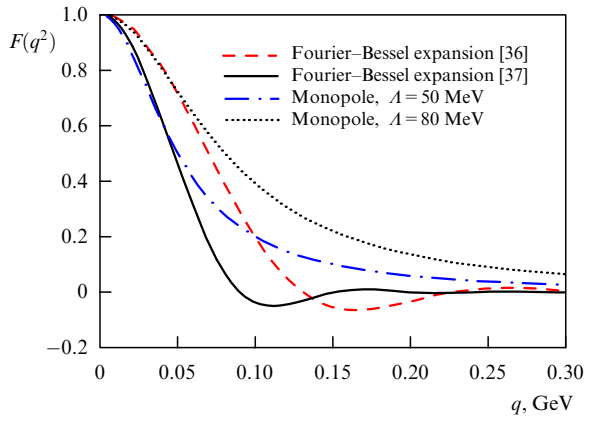

Figure 6. (Color online.) Published ^{208}Pb form factors and their approximations. The solid black curve and dashed red curve represent the form factors described in terms of Fourier–Bessel expansion (A.10). The expansion parameters a_n and R for the solid black curve are taken from [37], while for the dashed red curve, data from [36] are used. The blue dashed-dotted and green dotted lines are plotted for monopole form factors (A.11) with the respective parameters $\Lambda = 50$ MeV and $\Lambda = 80$ MeV.

Table 4. Parameters of the Fourier–Bessel expansion of the ^{208}Pb form factor.

Parameter	[36]*	[37]
R, fm	11.0	12.5
a_1	0.62732×10^{-1}	1.4396
a_2	0.38542×10^{-1}	-4.1850×10^{-1}
a_3	-0.55105×10^{-1}	-9.1763×10^{-2}
a_4	-0.26990×10^{-2}	6.8006×10^{-2}
a_5	0.31016×10^{-1}	2.6476×10^{-2}
a_6	-0.99486×10^{-2}	-1.5307×10^{-2}
a_7	-0.93012×10^{-2}	-7.1246×10^{-3}
a_8	0.76653×10^{-2}	2.7987×10^{-3}
a_9	0.20885×10^{-2}	2.3767×10^{-3}
a_{10}	-0.17840×10^{-2}	-1.0125×10^{-3}
a_{11}	0.74876×10^{-4}	-2.5836×10^{-4}
a_{12}	0.32278×10^{-3}	6.4297×10^{-5}
a_{13}	-0.11353×10^{-3}	6.5528×10^{-5}
a_{14}		1.4523×10^{-5}
a_{15}		-1.4430×10^{-5}

* Two sets of parameters are reported in [36]. The corresponding form factors almost coincide.

$\Lambda = 80$ MeV and form factors calculated using the Fourier–Bessel expansion parameters that have been selected in such a way that they describe experimental data available in 1987 [36] and 1995 [37] (see Table 4). For comparison, the same figure displays the monopole form factor with the parameter $\Lambda = 50$ MeV ($\hat{q} \approx 18$ MeV).

Appendix B. Pseudorapidity cutoff

To take into account the pseudorapidity cutoff, the ratio of photon energies $x = \omega_1/\omega_2$ should be expressed in terms of the invariant mass of the muon pair s, the muon transverse momentum p_T, and the muon pseudorapidity η. A collision of two photons with energies ω_1 and ω_2 is shown in Fig. 7. This collision produces μ^+ with a momentum p^+ and μ^- with a momentum p^-. It is assumed in what follows that $p_\mathrm{T} \gg m_\mu$ and the muon mass m_μ can be neglected; this is true for the experiments considered in this review.

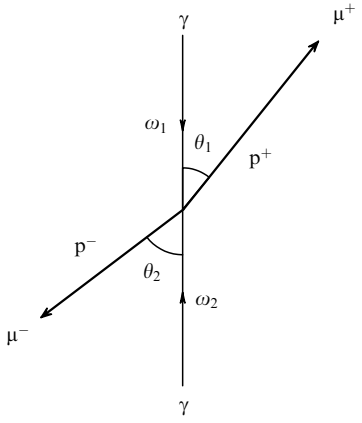

Figure 7. Reaction $\gamma\gamma \to \mu^+\mu^-$.

The energy–momentum conservation law yields

$$\begin{cases} p_\mathrm{T}^+ = -p_\mathrm{T}^- \equiv p_\mathrm{T}, \\ \omega_1 + \omega_2 = \sqrt{p_\mathrm{T}^2 + p_\parallel^{+2}} + \sqrt{p_\mathrm{T}^2 + p_\parallel^{-2}}, \\ \omega_1 - \omega_2 = p_\parallel^- - p_\parallel^+ . \end{cases} \tag{B.1}$$

The last two equations can be re-written in terms of the transverse momentum p_T and scattering angles θ_1 and θ_2:

$$\begin{cases} \dfrac{p_\mathrm{T}}{\sin\theta_1} + \dfrac{p_\mathrm{T}}{\sin\theta_2} = \omega_1 + \omega_2 , \\ \dfrac{p_\mathrm{T}}{\tan\theta_1} - \dfrac{p_\mathrm{T}}{\tan\theta_2} = \omega_1 - \omega_2 . \end{cases} \tag{B.2}$$

The scattering angles and pseudorapidity are related as

$$\eta_i = -\ln\tan\left(\frac{\theta_i}{2}\right), \quad i = 1, 2 , \tag{B.3}$$

whence,

$$\begin{cases} \cosh\eta_1 + \cosh\eta_2 = \dfrac{\omega_1 + \omega_2}{p_\mathrm{T}}, \\ \sinh\eta_1 - \sinh\eta_2 = \dfrac{\omega_1 - \omega_2}{p_\mathrm{T}} . \end{cases} \tag{B.4}$$

We now eliminate η_2 from this set of equations. We then have

$$\exp(2\eta_1) - \frac{2\omega_1}{p_\mathrm{T}}\exp(\eta_1) + \frac{\omega_1}{\omega_2} = 0 . \tag{B.5}$$

Having substituted $\omega_1 = \sqrt{sx/4}$ and $\omega_2 = \sqrt{s/4x}$, we arrive at

$$\exp(2\eta_1) - \frac{\sqrt{sx}}{p_\mathrm{T}}\exp(\eta_1) + x = 0 . \tag{B.6}$$

A solution of this equation for x is

$$\begin{aligned} x &= \exp(2\eta_1)\frac{\left(1 \pm \sqrt{1 - 4p_\mathrm{T}^2/s}\right)^2}{4p_\mathrm{T}^2/s} \\ &= \exp(2\eta_1)\frac{1 \pm \sqrt{1 - 4p_\mathrm{T}^2/s}}{1 \mp \sqrt{1 - 4p_\mathrm{T}^2/s}} . \end{aligned} \tag{B.7}$$

If η_1 varies within the range from $-\hat{\eta}$ to $\hat{\eta}$, x varies within the following limits:

$$\begin{cases} \exp(-2\hat{\eta})\dfrac{1+\sqrt{1-4p_\mathrm{T}^2/s}}{1-\sqrt{1-4p_\mathrm{T}^2/s}} < x < \exp(2\hat{\eta})\dfrac{1+\sqrt{1-4p_\mathrm{T}^2/s}}{1-\sqrt{1-4p_\mathrm{T}^2/s}}, \\ \exp(-2\hat{\eta})\dfrac{1-\sqrt{1-4p_\mathrm{T}^2/s}}{1+\sqrt{1-4p_\mathrm{T}^2/s}} < x < \exp(2\hat{\eta})\dfrac{1-\sqrt{1-4p_\mathrm{T}^2/s}}{1+\sqrt{1-4p_\mathrm{T}^2/s}}. \end{cases} \tag{B.8}$$

To satisfy both conditions $\eta_1 < |\hat{\eta}|$ and $\eta_2 < |\hat{\eta}|$, an overlap of these ranges should be selected. Therefore,

$$\frac{1}{\hat{x}} < x < \hat{x}, \quad \hat{x} = \exp(2\hat{\eta})\frac{1-\sqrt{1-4p_\mathrm{T}^2/s}}{1+\sqrt{1-4p_\mathrm{T}^2/s}}. \tag{B.9}$$

If these inequalities are used to determine the integration domain for the equivalent-photon spectrum, it must be checked that the photon energy does not exceed the cutoff energy $\hat{q}\gamma$:

$$\hat{x} < \frac{(2\hat{q}\gamma)^2}{s}. \tag{B.10}$$

This inequality always holds for the $\mathrm{pp}(\gamma\gamma) \to \mathrm{pp}\mu^+\mu^-$ reaction with constraints on the phase space imposed in [30]. However, in the case of the $\mathrm{Pb\,Pb}\,(\gamma\gamma) \to \mathrm{Pb\,Pb}\,\mu^+\mu^-$ reaction considered in [31], this inequality imposes an additional constraint on x, which should be taken into account in calculating the experimental cross sections using the equivalent photon approximation in the leading logarithmic approximation with a $\hat{q}$ cutoff.

Appendix C. Survival factor

It is well known that the distribution of equivalent photons in Eqn (2) can be found when considering the electromagnetic field generated by a rapidly moving charged particle. A solution of the Maxwell equations for the electromagnetic field of an ultrarelativistic particle moving along the z axis has the form [45, (33.2.3)]

$$\begin{aligned} \mathbf{E}_\perp(\mathbf{r},t) &= -\frac{\mathrm{i}Ze\gamma}{(2\pi)^3}\int\frac{\mathbf{q}_\perp}{\mathbf{q}^2}\exp\left[\mathrm{i}\mathbf{q}_\perp\mathbf{r}+\mathrm{i}\gamma q_z(z-vt)\right]\mathrm{d}^3q, \\ \mathbf{H}(\mathbf{r},t) &= \mathbf{v}\times\mathbf{E}(\mathbf{r},t), \end{aligned} \tag{C.1}$$

where $\mathbf{E}(\mathbf{r},t)$ and $\mathbf{H}(\mathbf{r},t)$ are the electric and magnetic fields at the point $\mathbf{r}$ at the moment t, $\mathbf{E}_\perp$ is the component of $\mathbf{E}$ perpendicular to the z axis, $\mathbf{v}$ is the particle velocity, and $\mathbf{q}$ is the Fourier transformation parameter.

The electric field component oriented along the z axis is not enhanced by the factor γ. Therefore, if $\gamma \gg 1$, the condition $E_\perp \gg E_z$ holds, and the electric field is almost entirely transverse, as it should be in the case of real photons. Equation (C.1) is therefore an expansion of the electromagnetic field into monochromatic plane waves with frequencies $\omega = v\gamma q_z \approx \gamma q_z$ that move along the z axis.

The total flux of electromagnetic energy along the z axis is given by the component of the Poynting vector

$$\Pi_z = \int \mathrm{d}^2b\int_{-\infty}^{\infty}\mathrm{d}t\,[\mathbf{E}\times\mathbf{H}]_z, \tag{C.2}$$

where $\mathbf{b} \equiv \mathbf{r}_\perp$ is the impact parameter of point $\mathbf{r}$. The quantity Π_z is equal to the total energy of equivalent photons:

$$\Pi_z = \int_0^\infty \omega\, n(\omega)\,\mathrm{d}\omega. \tag{C.3}$$

Substitution of expansion (C.1) in Eqn (C.2) yields

$$\begin{aligned} \Pi_z &= \int \mathrm{d}^2b\int\mathrm{d}t\,(E_x^2+E_y^2) \\ &= \frac{Z^2e^2\gamma^2}{(2\pi)^6}\int \mathrm{d}^2b\,\mathrm{d}t\,\mathrm{d}^3q\,\mathrm{d}^3q'\,\frac{-q_xq_x'-q_yq_y'}{\mathbf{q}^2\mathbf{q}'^2} \\ &\times\exp\left[\mathrm{i}x(q_x+q_x')+\mathrm{i}y(q_y+q_y')\right. \\ &\left.+\mathrm{i}\gamma(z-vt)(q_z+q_z')\right]F(\mathbf{q}^2)\,F(\mathbf{q}'^2), \end{aligned} \tag{C.4}$$

where the charged-particle form factor is taken into account. Integration with respect to d^2b and $\mathrm{d}t$ results in three delta-functions that are used to integrate with respect to d^3q'. We thus arrive at the formula

$$\Pi_z = \frac{Z^2\alpha\gamma}{2\pi^2}\int\frac{\mathbf{q}_\perp^2\,F^2(\mathbf{q}_\perp^2+\omega^2/\gamma^2)}{(\mathbf{q}_\perp^2+\omega^2/\gamma^2)^2}\,\mathrm{d}^3q. \tag{C.5}$$

Changing from the integration variable q_z to ω and comparing the derived formula with (C.3), we obtain

$$n(\omega)\,\mathrm{d}\omega = \frac{Z^2\alpha}{\pi^2}\int\frac{\mathbf{q}_\perp^2\,F^2(\mathbf{q}_\perp^2+\omega^2/\gamma^2)}{(\mathbf{q}_\perp^2+\omega^2/\gamma^2)^2}\,\mathrm{d}^2q_\perp\frac{\mathrm{d}\omega}{\omega}, \tag{C.6}$$

where an additional factor of 2 emerges because if q_z varies from $-\infty$ to $+\infty$, the variable ω spans the region $[0,\infty)$ twice. Equation (C.6) differs from formula (2) by taking the form factor into account.

To introduce the survival factor, the integral with respect to d^2b in (C.4) must be calculated last. We define the density of photons in the impact parameter space $n(\mathbf{b},\omega)$ as

$$n(\omega) = \int n(b,\omega)\,\mathrm{d}^2b. \tag{C.7}$$

Integrating (C.4) over $\mathrm{d}t$ and integrating over $\mathrm{d}q_z'$ using the delta-function, we obtain

$$\begin{aligned} n(b,\omega) &= \frac{Z^2\alpha}{4\pi^4\omega}\int\mathrm{d}\,q_\perp\mathrm{d}\theta\,\frac{q_\perp F(q_\perp^2+\omega^2/\gamma^2)}{q_\perp^2+\omega^2/\gamma^2} \\ &\times\int\mathrm{d}q_\perp'\mathrm{d}\theta'\,\frac{q_\perp' F(q_\perp'^2+\omega^2/\gamma^2)}{q_\perp'^2+\omega^2/\gamma^2}(-q_\perp q_\perp')\cos(\theta-\theta') \\ &\times\exp(\mathrm{i}bq_\perp\cos\theta)\exp(\mathrm{i}bq_\perp'\cos\theta'), \end{aligned} \tag{C.8}$$

where θ is the angle between $\mathbf{q}_\perp$ and $\mathbf{b}$ and θ' is the angle between $\mathbf{q}_\perp'$ and $\mathbf{b}$.

Using the integral representation of the Bessel function

$$\begin{aligned} &\int_0^{2\pi}\cos\theta\exp(\mathrm{i}a\cos\theta)\,\mathrm{d}\theta = 2\,\mathrm{i}\pi J_1(a), \\ &\int_0^{2\pi}\sin\theta\exp(\mathrm{i}a\cos\theta)\,\mathrm{d}\theta = 0 \end{aligned} \tag{C.9}$$

and the formula $\cos(\theta-\theta')=\cos\theta\cos\theta'+\sin\theta\sin\theta'$, we obtain

$$n(b,\omega)=\frac{Z^2\alpha}{\pi^2\omega}\left[\int \mathrm{d}q_\perp q_\perp^2\,\frac{F(q_\perp^2+\omega^2/\gamma^2)}{q_\perp^2+\omega^2/\gamma^2}J_1(bq_\perp)\right]^2. \quad \text{(C.10)}$$

A transition from (C.10) to (C.6) via (C.7) can easily be performed using the equality

$$\int_0^\infty J_1(ax)\,J_1(bx)\,x\,\mathrm{d}x=\frac{1}{a}\,\delta(a-b). \quad \text{(C.11)}$$

For a standalone particle, its finite transverse size is taken into account by the form factor F, which tends to zero as the transverse momentum $q_\perp$ increases. However, if an ultraperipheral collision of two charged particles is considered, we should require that the collision is indeed ultraperipheral, i.e., that the particles remain intact after the collision. In the case of high-energy hadrons, the particles can be approximated with black discs. Then the collision is ultraperipheral if the inequality $b\equiv|\mathbf{b}_1-\mathbf{b}_2|>2R$ is satisfied, where R is the transverse radius of a proton or a nucleus. To make the description more accurate, a function $P(b)$ can be introduced that is the probability that scattering with the impact parameter b is elastic. The cross section of state X production in ultraperipheral collisions then takes the form

$$\sigma(\mathrm{N\,N}\to\mathrm{N\,N\,X})=\int_0^\infty \mathrm{d}\omega_1\int_0^\infty \mathrm{d}\,\omega_2\,\sigma(\gamma\gamma\to\mathrm{X})$$
$$\times\int \mathrm{d}^2b_1\int \mathrm{d}^2b_2\,n(b_1,\omega_1)\,n(b_2,\omega_2)\,P(|\mathbf{b}_2-\mathbf{b}_1|), \quad \text{(C.12)}$$

where N denotes the colliding particles and $\sigma(\gamma\gamma\to\mathrm{X})$ is the X production cross section in the collision of two photons. For pointlike particles, $P(b)=1$ and

$$\sigma(\mathrm{N\,N}\to\mathrm{N\,N\,X})$$
$$=\int_0^\infty \mathrm{d}\omega_1\int_0^\infty \mathrm{d}\omega_2\,\sigma(\gamma\gamma\to\mathrm{X})\,n(\omega_1)\,n(\omega_2). \quad \text{(C.13)}$$

(The difference between Eqns (C.13) and (3) is that integrals with respect to ω_i are cut off in (C.13) by form factors, while in Eqn (3) they are cut off by introducing the parameter $\hat{q}$.) The survival factor is defined in [35] as

$$S_{\gamma\gamma}^2=\frac{\int_{b_1>R}\int_{b_2>R}n(b_1,\omega_1)\,n(b_2,\omega_2)\,P(|\mathbf{b}_2-\mathbf{b}_1|)\,\mathrm{d}^2b_1\,\mathrm{d}^2b_2}{\int_{b_1>0}\int_{b_2>0}n(b_1,\omega_1)\,n(b_2,\omega_2)\,\mathrm{d}^2b_1\,\mathrm{d}^2b_2}, \quad \text{(C.14)}$$

where R is the radius of colliding particles. Because the form factor $F(q_\perp^2+\omega^2/\gamma^2)$ cuts off the integral in Eqn (C.10) at large $q_\perp$ or small b, integration in the numerator should not additionally exclude regions where b_1 or b_2 is small. Therefore, we propose the following formula for the survival factor of ultraperipheral scattering:

$$S_{\gamma\gamma}^2=\frac{\int_{b_1>0}\int_{b_2>0}n(b_1,\omega_1)\,n(b_2,\omega_2)\,P(|\mathbf{b}_2-\mathbf{b}_1|)\,\mathrm{d}^2b_1\,\mathrm{d}^2b_2}{n(\omega_1)\,n(\omega_2)}. \quad \text{(C.15)}$$

References

1. Landau L D, Lifshitz E M *Phys. Z. Sowjetunion* **6** 244 (1934); Translated into Russian: in Landau L D *Sobranie Trudov* (Collected Works) Vol. 1 (Moscow: Nauka, 1969) p. 110
2. Bertulani C A, Baur G *Phys. Rep.* **163** 299 (1988)
3. Baur G et al. *Phys. Rep.* **364** 359 (2002); hep-ph/0112211
4. Baur G, in *Electromagnetic Probes of Fundamental Physics, October 16–21, 2001, Erice, Italy, The Workshop* (The Science and Culture Series Physics, Vol. 22, Eds W J Marciano, S White) (River Edge: World Scientific, 2003) p. 183; hep-ph/0112239
5. Baur G et al., in *Electromagnetic Probes of Fundamental Physics, October 16–21, 2001, Erice, Italy, The Workshop* (The Science and Culture Series Physics, Vol. 22, Eds W J Marciano, S White) (River Edge: World Scientific, 2003) p. 235; hep-ex/0201034
6. Frankfurt L, Strikman M, Zhalov M *Acta Phys. Polon. B* **34** 3215 (2003); hep-ph/0304301
7. Bertulani C A, Klein S R, Nystrand J *Annu. Rev. Nucl. Part. Sci.* **55** 271 (2005); nucl-ex/0502005
8. Nystrand J *Nucl. Phys. A* **787** 29 (2007); hep-ph/0611042
9. Baltz A J et al. *Phys. Rep.* **458** 1 (2008); arXiv:0706.3356
10. Baur G *Eur. Phys. J. D* **55** 265 (2009); arXiv:0810.1400
11. Klusek-Gawenda M, Szczurek A *Phys. Lett. B* **700** 322 (2011); arXiv:1104.0571
12. Szczurek A *Acta Phys. Polon. B* **45** 1597 (2014); arXiv:1404.0896
13. Klusek-Gawenda M, Lebiedowicz P, Szczurek A *Phys. Rev. C* **93** 044907 (2016); arXiv:1601.07001
14. Klusek-Gawenda M, Szczurek A *Phys. Lett. B* **763** 416 (2016); arXiv:1607.05095
15. Gay Ducati M B et al. *Phys. Rev. D* **94** 094023 (2016); arXiv:1610.06647
16. Klusek-Gawenda M et al. *Phys. Rev. D* **96** 094029 (2017); arXiv:1708.09836
17. Adamczyk L et al. (The ATLAS Collab.) "Technical Design Report for the ATLAS Forward Proton Detector", CERN-LHCC-2015-009, ATLAS-TDR-024-2015 (Geneva: CERN, 2015)
18. Albrow M et al. (The CMS and TOTEM Collab.) "CMS-TOTEM Precision Proton Spectrometer", CERN-LHCC-2014-021, TOTEM-TDR-003, CMS-TDR-13 (Geneva: CERN, 2014)
19. Public CMS Luminosity Information, https://twiki.cern.ch/twiki/bin/view/CMSPublic/LumiPublicResults
20. LuminosityPublicResultsRun2, https://twiki.cern.ch/twiki/bin/view/AtlasPublic/LuminosityPublicResultsRun2
21. Jowett J M et al., in *7th Intern. Particle Accelerator Conf., IPAC'16, Busan, Korea, 8 – 13 May 2016* (Eds K S Kim et al.) (Geneva: JACoW, 2016)
22. Fermi E *Z. Phys.* **29** 315 (1924)
23. Weizsäcker C F V *Z. Phys.* **88** 612 (1934)
24. Williams E J *Kgl. Danske Vidensk. Selskab. Mat.-Fiz. Medd.* **13** 4 (1935)
25. Balakin V E, Budnev V M, Ginzburg I F *JETP Lett.* **11** 388 (1970); *Pis'ma Zh. Eksp. Teor. Fiz.* **11** 559 (1970)
26. Terazawa H *Rev. Mod. Phys.* **45** 615 (1973)
27. Budnev V M et al. *Fiz. Elem. Chast. Atom. Yadra* **4** 239 (1973)
28. Budnev V M et al. *Phys. Rep.* **15** 181 (1975)
29. Harland-Lang L A, Khoze V A, Ryskin M G *Eur. Phys. J. C* **76** 9 (2016); arXiv:1508.02718
30. Aaboud M et al. (The ATLAS Collab.) *Phys. Lett. B* **777** 303 (2018); arXiv:1708.04053
31. The ATLAS Collab., ATLAS-CONF-2016-025 (2016)
32. Breit G, Wheeler J A *Phys. Rev.* **46** 1087 (1934)
33. Brodsky S J, Kinoshita T, Terazawa H *Phys. Rev. D* **4** 1532 (1971)
34. Berestetskii V B, Lifshitz E M, Pitaevskii L *Quantum Electrodynamics* (Oxford: Pergamon Press, 1982); Translated from Russian: *Kvantovaya Elektrodinamika* (Moscow: Nauka, 1989)
35. Dyndal M, Schoeffel L *Phys. Lett. B* **741** 66 (2015); arXiv:1410.2983
36. De Vries H, De Jager C W, De Vries C *Atom. Data. Nucl. Data Tabl.* **36** 495 (1987)
37. Fricke G et al. *Atom. Data. Nucl. Data Tabl.* **60** 177 (1995)
38. Hencken K, Kuraev E A, Serbo V G *Phys. Rev. C* **75** 034903 (2007)
39. Baltz A J *Phys. Rev. C* **80** 034901 (2009); arXiv:0901.0891

40. Jentschura U D, Serbo V G *Eur. Phys. J. C* **64** 309 (2009); arXiv:0908.3853
41. Klein S R et al. *Comput. Phys. Commun.* **212** 258 (2017)
42. Patrignani C et al. (Particle Data Group) *Chinese Phys. C* **40** 100001 (2016)
43. Pacetti S, Ferroli R B, Tomasi-Gustafsson E *Phys. Rep.* **550 – 551** 1 (2015)
44. Dreher B et al. *Nucl. Phys. A* **235** 219 (1974)
45. Akhiezer A I, Berestetskii V B *Quantum Electrodynamics* (New York: Interscience Publ., 1965); Translated from Russian: *Kvantovaya Elektrodinamika* (Moscow: Nauka, 1969)